Suspension dynamics in transitional pipe flow

Willian Hogendoorn [1] Bidhan Chandra [1,2] and Christian Poelma [1,*]

[1]*Delft University of Technology, Multiphase Systems (3ME-P&E), Leeghwaterstraat 39, 2628 CB Delft, The Netherlands*

[2]*Indian Institute of Science Education & Research, Chemical Engineering, Bhopal 462066, India*

Particle-laden pipe flows exhibit a gradual laminar-turbulent transition, beyond a critical volume fraction (ϕ). While classical transition behavior is characterized by the presence of turbulent puffs, this intermittent nature is absent for particle-induced transition. For small pipe-to-particle diameter ratios (D/d) even dilute systems exhibit this particle-induced transition behavior. In this study we use neutrally buoyant particles with a D/d of 5.7, which represents a "sweet spot," allowing the use of particle image velocimetry to study this particular phenomenon. The average velocity profile gradually changes from a parabola (laminar flow) to a blunted velocity profile for increasing Reynolds number. The instantaneous velocity profiles fluctuate around this profile. These velocity fluctuations, described by u_x-rms and u_r-rms, gradually increase for increasing Reynolds number, as do the Reynolds stresses. For low Re_s, the velocity fluctuations increase proportional to the bulk velocity, which can be explained by a simple model based on the finite size of the particles. The velocity fields show the presence of elongated streamwise structures. The largest length scales are found in the transition region, where average integral length scales up to $5D$ are found. The structures decrease in length when the flow has fully transitioned to a turbulent state.

I. INTRODUCTION

Suspensions are present in a wide variety of applications, such as blood flow, food processing, and dredging. Despite their importance, the behavior of these suspensions is not fully understood. In particular, the way a flowing suspension transitions from a laminar to a turbulent state is an open question. This flow state has important practical implications, especially as it dictates the pressure losses for a given flow rate. This sets the motivation for this study.

Laminar-turbulent transition in pipe flow has been a topic of extensive research since the ink experiments by Reynolds in the early 1880s [1]. His celebrated result showed that below a critical velocity the flow remains in a laminar state. Above this critical velocity, Reynolds observed "flashes," which are nowadays referred to as turbulent patches or puffs. For even higher flow velocities the flow was found to be fully turbulent. Turbulent puffs are nowadays known to have increasing characteristic lifetimes for an increasing Reynolds number ($\mathrm{Re} = UD/\nu$, with U the bulk velocity of the fluid, D the pipe diameter, and ν the kinematic viscosity of the fluid) [2,3]. Based on experimental and numerical data, Avila *et al.* [4] showed that the critical point for sustained turbulence (i.e., the point where these puffs grow and split) is at an approximate Reynolds number of 2040. This provided physical insight in the empirical result originally obtained by Reynolds.

---

*c.poelma@tudelft.nl

064301-1

Thanks to enormous research efforts, single-phase laminar-turbulent transition is understood in considerable detail, despite some open questions. In contrast, less attention has been given to the effect of non-Brownian particles, i.e., particles with diameters (d) exceeding 1 μm, on this transition behavior. Pioneering experiments with particle-laden pipe flows were reported by Murthy and Zandi [5], followed by the study of Mih [6] in the late sixties and seventies, respectively. However, both studies are performed for fully developed turbulent flows, well away from the transition region. The first detailed study investigating the effect of particles on the laminar-turbulent transition was conducted by Abbas and Crowe [7] in 1987. For an increasing particle concentration, they observed a frictional drag increase for turbulent flows. Apart from this observation, they reported that the presence of particles did *not* influence the transition behavior. However, seemingly no viscosity correction was applied to compensate for the presence of the particles. Adding particles to a fluid will increase the apparent (or suspension) viscosity, as was theoretically shown in the famous work by Einstein in 1911 [8]. Park *et al.* [9] performed particle-laden pipe flow experiments in the transition region. Using refractive index matching they were able to extract velocity information by means of laser Doppler anemometry measurements. The suspension used was composed of a Stoddard solvent (60%) and a mineral oil (40%) to which they added particles (14% based on volume). Yield-power-law behavior was observed for this particular slurry. Normally this non-Newtonian behavior is expected only for higher volume fractions [10], so it is uncertain whether this was due to the particles or the suspending fluids that were used (or a combination of both). They concluded that the transition region is much narrower (in Re) for this non-Newtonian suspension as compared to a single-phase flow. Again, in this study it is not explicitly stated whether a viscosity correction is applied or not.

The first study showing a prominent effect of particles on laminar-turbulent transition was reported by Matas *et al.* [11] in 2003. By measuring the low-frequency pressure fluctuations, which are indicative of the presence of turbulent puffs, they were able to determine the critical Reynolds number for various concentrations. The Reynolds number in their study was based on the corrected viscosity using Kriegers' model [10] to account for the presence of particles. They conducted an extensive study in which the pipe-to-particle diameter ratio (D/d) was varied. For particles with $D/d \leqslant 65$, the critical Reynolds number was found to depend on the particle volume fraction (ϕ). For particle concentrations below 25% an earlier onset to transition was found compared to single-phase flow. In this regime, D/d strongly affected the critical Reynolds number: for a fixed concentration, larger particles caused a lower critical Reynolds number. For $D/d \geqslant 65$, no effect of the particles on the transition was found, until a volume fraction of 25%. Above this volume fraction limited data were available, so no definitive conclusions could be drawn. The general trends of this transition behavior were confirmed by the numerical simulations performed by Yu *et al.* [12]. Recently, Hogendoorn and Poelma [13] provided more insight in transitional particle-laden flows, based on ultrasound imaging velocimetry and pressure drop measurements. For relatively high volume fractions ($\phi > 17.5\%$) the transition scenario was found to be distinctly different from the single-phase transition. A smooth, particle-induced transition was found, with the apparent absence of turbulent puffs in the transition region. The friction factor for lower Reynolds numbers was found to collapse on 64/Re (i.e., Poiseuille's law), once corrected for the enhanced viscosity. This particle-induced transition behavior for higher particle concentrations was independently found by Agrawal *et al.* [14]. Very recently, Leskovec *et al.* [15] performed experiments with large spherical and cubic particles ($D/d \leqslant 5.9$). Using a model, balancing particle-agitation and fluid dissipation, they distinguish between classical and smooth transition (i.e., particle-induced in our terminology).

Little is known about the nature of this particle-induced transition behavior. This is mainly because (nonintrusive) measurements in suspensions are difficult to perform due to the opaque nature of these flows [16]. Fully resolved numerical simulations are feasible in principle [17], but the long simulation times required for convergence in the transition region make them currently prohibitively expensive. The objective of the current study is to investigate this particle-induced transition using particle image velocimetry (PIV). For the general case this is not feasible, but we identified a case that exhibits particle-induced transition, while still having a particle concentration
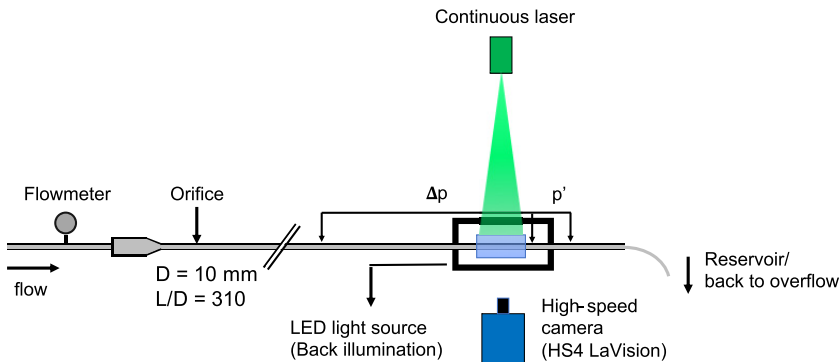
FIG. 1. Schematic of the experimental setup. The pipe is enclosed in a rectangular optical box at the measurement location to minimize optical distortion.

low enough to perform optical measurements. Preliminary experiments based on pressure drop measurements showed a strong dependency on the D/d ratio, in line with the observations of Matas *et al.* [11]. For small D/d ratios even dilute systems exhibited this particle-induced transition behavior, while still maintaining sufficient optical access. Our study uses a pipe-to-particle diameter ratio of 5.7, which presents a "sweet spot" allowing use of PIV to study this particular phenomenon.

Particle-induced transition has previously been studied to some extent using ultrasound imaging velocimetry [13]. The data in that study allowed only a qualitative description of the change in transition mechanism, rather than a quantitative description of the flow. In the present study we provide a detailed description of this particle-induced transition based on instantaneous velocity fields of the fluid.

The structure of this paper is as follows: in Sec. II the experimental facility is described, including the experimental procedure and the PIV setup. In Sec. III the method for the processing of the measurement data is presented, as well as the validation of the PIV measurements. The results can be found in Sec. IV. This paper ends with a discussion and conclusion in Secs. V and VI, respectively.

II. EXPERIMENTAL DETAILS

A. Experimental facility

Experiments are performed in a slightly adapted version of the setup described in Hogendoorn and Poelma [13]. This setup consists of a 10.00 mm diameter (D) precision glass pipe with a total length (L) of 310D after the trigger mechanism. The flow is pressure driven by means of an overflow tank. The height of this tank can be adjusted to control the Reynolds number. The Reynolds number is here defined as Re $= \rho U_b D / \mu_s$, where ρ is the density of the fluid, U_b is the bulk velocity, and μ_s is the dynamic viscosity of the suspension. By using a settling chamber and smooth contraction, a laminar flow is maintained to Reynolds numbers higher than 4000 for the single-phase case. An orifice plate (inner diameter, $d_i = 7.5$ mm), comparable with Wygnanski and Champagne [18], is used as a trigger mechanism to ensure a fixed transition around a Reynolds number of 2000. After this trigger there is a development length of 125D, followed by the measurement section. A schematic of this measurement section is shown in Fig. 1. First, a pressure drop measurement (Validyne DP45) over 125D is obtained, indicated by Δp. Another differential pressure drop measurement is performed over 5D, by which the local pressure fluctuations (p') are measured. At 220D the (local) particle concentration and the flow fields are obtained. The particle concentration is determined using a camera (the same as will be used for PIV; see Sec. II C) in combination with LED back-illumination. The temperature is monitored in the downstream collection reservoir.

The viscosity of the water is corrected accordingly. The temperature change during one single measurement is negligible to have an effect on the Reynolds number ($\Delta T < 0.1$ K).

The particles used as dispersed phase are unexpanded polystyrene particles (SynthosEPS, Breda, The Netherlands) with a diameter $d = 1.75 \pm 0.12$ mm. This corresponds to a pipe-to-particle diameter ratio of 5.7, which means that these particles act as relatively big "obstacles" (flow blockage ratio of 3%). The density of these particles is determined to be $\rho = 1032 \pm 1.17$ kg/m^3. Salt (Na$_2$SO$_4$) is added to the water to match the densities of the fluid and the polystyrene particles. The viscosity of the salt water mixture is corrected accordingly [19].

B. Experimental procedure

The desired Reynolds number is prescribed by changing the height of the overflow reservoir, using an in-line flow meter for monitoring. The actual volumetric flow rate is determined by measuring the time it takes to collect a given volume of suspension from the outflow of the pipe. Using this method, the Reynolds number can be determined with an uncertainty smaller than 0.5%.

The average particle concentration for *low* volume fractions is determined from the camera images. For this the experimental setup is operated at the desired Reynolds number and sufficient statistically independent images are acquired with LED back-illumination only. Using an automated image processing script implemented in Matlab [20] to count the number of particles per image, the concentration (ϕ) is retrieved. For concentrations higher than 1% particle counting is no longer feasible, but for these cases the volume fraction can be determined accurately by weighing the amount of particles and fluid when preparing the suspension. The suspension viscosity is then determined using Eilers' viscosity model [10]:

$$\frac{\mu_s}{\mu_0} = \left(1 + 1.25\frac{\phi}{1 - \phi/0.64}\right)^2, \tag{1}$$

where μ_0 is the viscosity of the continuous phase (i.e., saline water).

For the measurements, the camera recording is triggered at the same time as the pressure acquisition. The sample frequency of the camera is adjusted depending on the Reynolds number. This way the maximum streamwise particle displacement between subsequent images is in the order of 10 pixels to ensure good correlation [21]. The camera memory allows for a maximum of 48 000 images, which corresponds to single data set lengths varying between 30 and 60 s.

C. PIV setup

PIV measurements are performed using a high-speed CMOS camera (Imager HS 4M, LaVision). This camera is equipped with a 105 mm Nikon Micro-Nikkor objective using an aperture of $f^{\#} = 5.6$ and a magnification of 0.18. The field of view is set to 2016×248 pixels, corresponding to 120.7×14.9 mm^2.

The flow is seeded with hollow glass spheres (Sphericel 110P8, Potter Industries). The mean diameter of these particles is 12 μm, and they have a density of 1.1 ± 0.5 g/cm^3. No effect of these particles was observed on the transition behavior (i.e., the transition curves with and without tracer particles were in agreement with each other). For illumination a continuous laser (PEGASUS, PL.M525.1300) is used, operated at 80% of its maximum power. The laser light sheet enters from above and is located perpendicular to the camera, illuminating the center plane of the pipe. The LED and laser intensities are approximately matched, such that both the PIV tracer particles and the larger polystyrene particles are visible in the same camera image.

III. DATA PROCESSING

A. PIV processing and validation

The PIV images are processed using a well-established in-house code, based on Westerweel [22]. This code is a multipass, FFT correlation-based algorithm, programmed in Matlab [20]. Universal outlier detection is applied and outliers (generally less than 2%) are replaced by linear interpolation [23]. A double-pass PIV interrogation on subsequent images is performed using interrogation window sizes of [24 × 64] and [12 × 32] pixels. For both cases 50% overlap is used, which gives a final spatial resolution of 0.36×0.96 mm^2 (radial×streamwise). This resolution is small compared to the dispersed phase particles, therefore the vectors at the particle locations have to be filtered out. The procedure for this filtering will be described later (see Sec. III C). The final velocity fields span 37×123 vectors. These full vector fields were used to visualize the flow (see also the supplemental movies [24]), while the profile statistics are based on the 100th vector column of each field. No significant differences were found if other columns were used.

Both the single-phase and the multiphase PIV results are validated. The single-phase PIV data are validated by comparing a turbulent case (Re = 5300) to the reference data from Eggels *et al.* [25]. A good agreement is found for the mean velocity profile (average error less than 0.5%) as well as for the u_x-rms and u_r-rms values (error less than 2.5% and 10%, respectively). However, no reference solution is available for the particle-laden cases. Therefore, these cases are validated by integrating the average velocity profiles and comparing these with the volume flow obtained from the pipe exit. For low Reynolds numbers (e.g., Re < 1600) the PIV data overestimate the volume flow by 1.3%. This overestimation increases for higher Reynolds numbers. This increasing overestimation is explained by the stronger velocity gradients in the near-wall region, which are not fully resolved for higher Reynolds numbers. Furthermore, these near-wall regions have a high contribution to the velocity integral (rdr), which causes small errors to be amplified. In conclusion, the PIV data are considered to give a reliable result of the flow fields.

B. Signal-to-noise ratio

The noise in the velocity data can be quantified using the autocorrelation function [26]. This utilizes the fact that flow structures are correlated (i.e., they have a certain length scale) and measurement noise is generally not correlated. This means that only the value at the ordinate axis of the autocorrelation function contains the contribution of noise, while the rest of the correlation function is unaffected. Furthermore, for homogeneous isotropic turbulence the shape of the correlation function (for $t \to 0$) can be approximated by a parabola [27]. The difference between the value at the ordinate axis and the extrapolated maximum of this parabola is the contribution by the noise (see, e.g., Hogendoorn and Poelma [28] for an application of this method to obtain reliable turbulence statistics from noisy data). For a representative case the error in the statistics was found to be well below 5%, with small variations across the radius of the pipe. For the higher Reynolds number experiments the spatial and/or temporal resolution were insufficient to accurately fit a parabola.[1] Nevertheless, as these experiments use the same measurement system and PIV settings (particle displacement, etc.) the aforementioned error can serve as a good reference value. As the estimated error is relatively small, no noise removal was attempted.

C. Particle masking in PIV data

As mentioned earlier, the dispersed particles cover multiple interrogation areas. Masking can be performed on the raw images or on the vector fields. The former is computationally much more expensive as particles need to be detected. This is further complicated by their change in appearance

---

[1]Note that the inability to resolve the microscales does not mean that we cannot measure flow statistics accurately, as most of the energy-containing scales are captured.
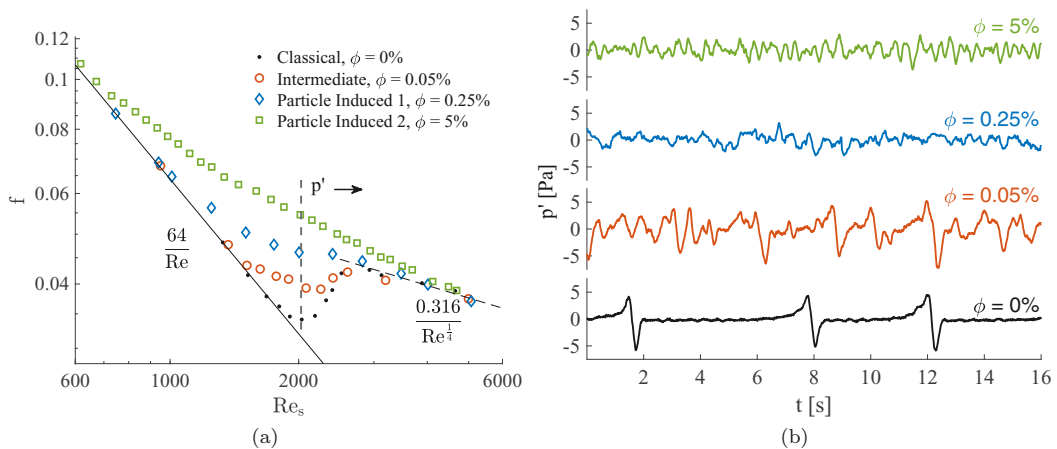
FIG. 2. (a) Friction factor as a function of suspension Reynolds number for four volume fractions. (b) Corresponding pressure signatures from the small distance pressure sensor, p', for various concentrations and similar suspension Reynolds number ($\mathrm{Re}_s \approx 2000$).

as they move along the optical axis (e.g., from within the light sheet to the near wall region). For this reason it is decided to mask the particles in the vector fields, as patches of erroneous vectors (caused by the particle) are readily detected. This is done using the following thresholding method: A moving standard deviation is calculated using seven entries in the velocity time series at each location. If the moving standard deviation exceeds a threshold (in this case the standard deviation of the total signal) these values are omitted from further analysis. This method was verified by comparing the outcome to results based on manual filtering (i.e., by visual inspection of the raw images). A negligible difference between the two autocorrelation functions was found, which is indicative that the thresholding method is appropriate. As the masking process results in gaps in the velocity data, the autocorrelation function is explicitly calculated using the so-called slotting method (see e.g., [29,30]). This avoids artifacts due to interpolation.

IV. RESULTS

Four different transition scenarios are shown in Fig. 2(a), where the Darcy friction factor, $f = \Delta p / (\frac{1}{2} \rho U_b^2 L / D)$, is shown as a function of the (suspension) Reynolds number. The four cases shown have a particle concentration of $\phi = 0$, 0.05%, 0.25%, and 5%. Throughout this study we will refer to these cases as "classical," "intermediate," "particle-induced 1," and "particle-induced 2," respectively. In this study we define a transition characterized by isolated puff signatures as *classical* transition. *Particle-induced* transition is characterized by continuous velocity (or pressure) fluctuations with the absence of puff signatures, as will be shown later. In this regime the friction factor monotonically decreases for increasing Reynolds number. In the *intermediate* transition, characteristics from both scenarios can be observed (puffs *and* continuous fluctuations); this is the case for $\phi = 0.05\%$. For the first three cases (classical, intermediate, and particle-induced 1), PIV data are available in addition to pressure drop data (Δp, p'). In Fig. 2(b) four different excerpts of time series are shown. These are obtained using the small distance pressure sensor, p'. These series correspond to the cases in Fig. 2(a), which are indicated by the vertical, dashed line at Reynolds ≈ 2000 (labeled p'). Note that the small distance pressure sensor is used to capture pressure fluctuations, while the long-distance pressure sensor is used for average pressure drop measurements. For this reason the mean-subtracted signal is shown. For visualization purposes, a mild filter is applied (convolution with a Hanning function, $\Delta t = 20$ ms) to eliminate high-frequency noise. From both figures, the change in transition behavior is evident, but this change can best be explained using
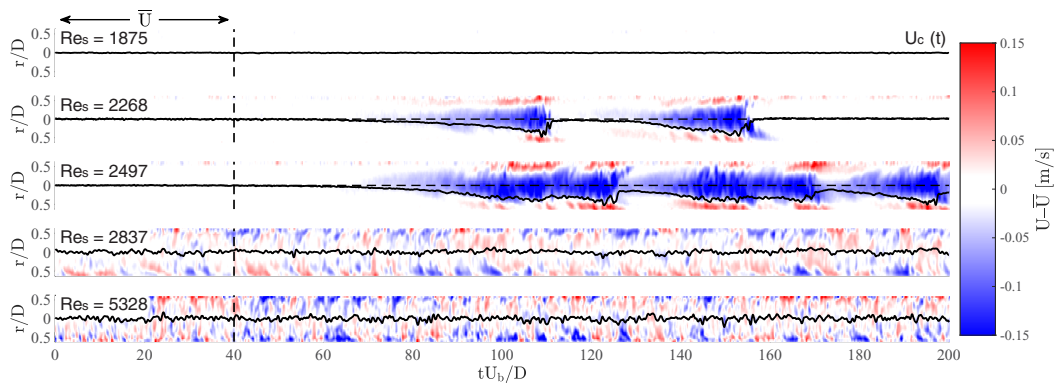
FIG. 3. Five characteristic results for a classical, single-phase transition scenario ($\phi = 0$). The streamwise velocity patterns, u'_x, are shown as a function of dimensionless distance tU_b/D for various Reynolds numbers.

Fig. 2(b). For $\phi = 0\%$, classical puffs can be observed for $t \approx 2$, 8, and 12 s. For increasing particle concentration ($\phi = 0.05\%$), these typical puff signatures are still visible (e.g., $t \approx 12$ s). In addition, continuous fluctuations are observed due to the presence of particles (this will be shown later using PIV results). For the particle-induced cases no distinct puffs are present in the pressure signal. Puffs are also absent for lower or higher values of Re_s, so this is not simply the result of an earlier onset of the transition. These results resemble findings from our earlier study [13], but they are shown here to facilitate the subsequent analysis.

A. Transition behavior for single-phase flow

The main focus of this paper is to provide insight into the particle-induced transition. This particle-induced transition behavior will be compared and contrasted to classical transition behavior. In this section the general transition behavior for single-phase flow will be shown, which serves as a reference for the particle-laden transition cases.

The velocity data are decomposed in a mean ($\bar{U}$) and a fluctuation (u') using Reynolds decomposition. Here U is the streamwise velocity component. As the mean radial velocity component is zero we have omitted the subscript "x" for brevity. The streamwise and radial velocity fluctuations are indicated with subscripts "x" and "r," respectively. In Fig. 3 we show five typical results for a classical, single-phase transition scenario. Here the streamwise velocity fluctuations (u'_x) are shown for various Reynolds numbers as a function of dimensionless distance, tU_b/D. The mean velocity profile used for the decomposition is based on an average of $tU_b/D = 0 - 40$, as indicated by $\bar{U}$ in the top left of the figures (Figs. 3–5). For all velocity series, $40tU_b/D$ was found to be sufficient for statistical convergence of the mean for these visualizations. For the first three cases this results in a laminar (parabolic) velocity profile, which is subtracted to visually enhance the appearance of the turbulent structures in the flow. For the latter two cases a turbulent (i.e., a more flattened) velocity profile is subtracted as no laminar regions are present. The instantaneous centerline velocity ($U_c(t)$) is superimposed on all five cases. For visualization a mild filter (convolution with a 3×7 kernel) is applied to the vector fields to remove high-frequency measurement noise. Note that this filter size is small compared to the structures that can be observed.

Figure 3 shows how a laminar flow (Re = 1875, panel 1) transitions to a turbulent flow. The onset to turbulence for classical transition is characterized by the appearance of localized turbulent patches embedded in a laminar flow. These puffs can be seen in panel 2 for $tU_b/D = 100$ and 140. The quantity of these puffs is increasing for increasing Reynolds number, which can be seen in the third panel. This process continues until the complete pipe is filled with turbulent structures (see panels 4 and 5).
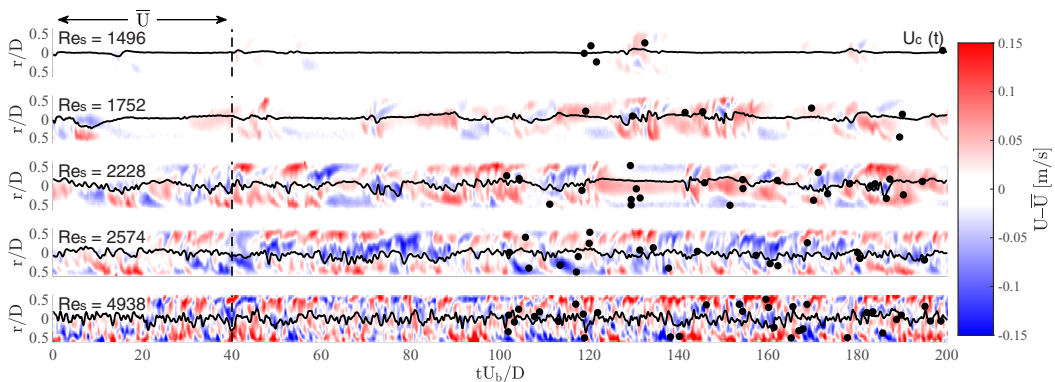
FIG. 4. Streamwise velocity patterns (u'_x) as a function of time for various Reynolds numbers. The concentration for this case is $\phi = 0.05\%$. Particles are shown only for the second part of the time series ($tU_b/D > 100$).

B. Intermediate transition behavior

The second transition curve in the Moody diagram [Fig. 2(a), open circles] is an intermediate transition scenario, obtained for a particle concentration, $\phi = 0.05\%$. Due to this low volume fraction, statistical fluctuations in the spatial particle distribution are significant: in the measurement volume (spanning $12D$), typically between zero and six particles are present. Based on the temporal particle distribution within the total measurement volume, a Poisson distribution is fitted with constant, $\lambda = 1.9$. This corresponds to 0.17 particles per $1D$ pipe length on average. In Fig. 4 five representative streamwise velocity patterns are shown for increasing Reynolds numbers. These are visualized using the same approach as the single-phase case.

For $tU_b/D > 100$, particles are superimposed on the velocity map. The position of the particles is indicative of their actual position within one particle diameter. Note that all particles in the pipe are shown (i.e., irrespective of their position along the optical axis), whereas the velocity fields are measured in the center plane of the pipe. With respect to the classical transition scenario, some differences can be observed. The friction factor for the first case ($Re_s = 1496$) is slightly higher than 64/Re [see Fig. 2(a)]. However, for this case isolated velocity fluctuations are present, rather than typical puff signatures. For some locations, these fluctuations coincide with the presence of particles (see, e.g., $tU_b/D = 130$). For other locations, fluctuations can be observed in absence of particles (see, e.g., $tU_b/D = 180$). Also in the second and third panels, no typical puff signatures can be observed (i.e., the characteristic "sawtooth" shape in the streamwise velocity component, as in Fig. 3, panel 2). For both cases confined laminar regions are observed, for instance, in the second and third panel for $tU_b/D \approx 60$ and 135, respectively. The fraction of these confined laminar regions decreases for increasing Reynolds number. These laminar regions are absent in the final two panels, where the flow state is turbulent. Note that the entire transition occurs for lower Re_s, confirming the well-established effect of relatively large particles [11].

It is important to note that the velocity fluctuations in the first panel ($Re_s = 1496$) are not (decaying) puffs, created by the orifice located at the beginning of the pipe. For this case, the average travel distance before puffs decay is in the order of $35D$ [3,4], whereas the distance between the orifice and the current measurement location is 220D.[2] The particles are thus likely responsible for the velocity fluctuations, despite the fact that particle locations here do not appear to correlate with the fluctuations (as will be discussed in Sec. V).

————

[2]For higher Reynolds number ($Re \geqslant 1700$) puffs created by the orifice travel generally $\geqslant 220D$ before they decay.
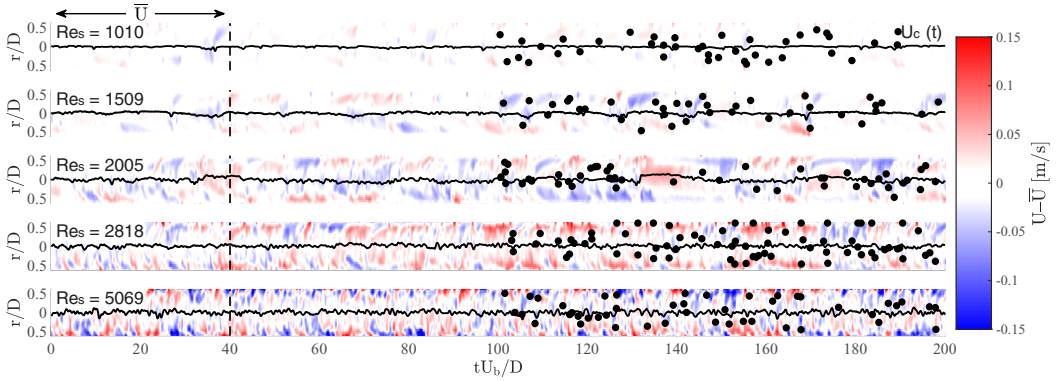
FIG. 5. Streamwise velocity patterns (u'_x) as a function of time for various Reynolds numbers. The concentration for this case is $\phi = 0.25\%$. Particles are shown only for the second part of the time series ($tU_b/D > 100$).

C. Particle-induced transition behavior

In this section the particle-induced transition scenario will be discussed in more detail [the transition curve with the blue diamond markers in Fig. 2(a)]. For this transition case it is still feasible to obtain reliable PIV results because of the low enough particle concentration. For this concentration ($\phi = 0.25\%$) the number of particles in the camera images ($12D$) is described by a Poisson distribution with $\lambda = 11.1$. This corresponds to 0.9 particles per $1D$ pipe length on average. Five characteristic velocity patterns are shown in Fig. 5. Also for this case the particles are superimposed on the time series for $tU_b/D > 100$. For all Reynolds numbers velocity fluctuations are present, as can be seen from the superimposed centerline velocities, or from the color map indicating the streamwise velocity fluctuations. The fluctuation intensity [see also Fig. 9(a) below] increases for increasing Reynolds number, which is evidence for the gradual transition induced by the particles.

Three different centerline velocity probability distribution functions (PDFs) for constant Reynolds number ($\mathrm{Re}_s \approx 2000$) are shown in Fig. 6(a). Here the centerline velocity is normalized using the bulk velocity. A fully developed laminar flow would be represented by a narrow peak at $\bar{U}_c/U_b = 2$. The presence of turbulent puffs or structures alters this probability distribution. This can be seen from the PDF for the classical case, where puffs are represented by the tail on the left-hand side of the distribution (see, e.g., the centerline velocity in Fig. 3, panel 2). For increasing volume fraction the first moment of the distribution shifts to lower normalized velocities. This shows the change in the (mean) velocity profile, which is directly related to the flow state. The PDF from the particle-induced case (square yellow markers) is separately shown in Fig. 6(b). An interesting observation is the bimodal distribution, which can be approximated by adding two Gaussian curves (indicated by dashed lines). Based on visual inspection of the flow fields, the right-hand side can be attributed to isolated patches of "laminar-like" flow (see, e.g., Fig. 5, panel 3, $tU_b/D = 140$). The left-hand side of the distribution can be attributed to the turbulent structures that make up the majority of the flow. The envelope of both these distributions is given by the black continuous line. The area ratio of both distributions (1:7.8) is in approximate agreement with the fraction of "laminar" patches observed in the corresponding time series. From the right-hand side Gaussian PDF it can be seen that these "laminar-like" patches do not fully recover to laminar flow (i.e., parabolic velocity profile with $\bar{U}_c/U_b = 2$). Based on bimodal curve fitting, the mean velocity of these patches is found to be 1.81 ± 0.05. The fact that these "laminar" regions do not recover to full laminar flow is most likely due to the limited available time before the flow is perturbed again by the particles.
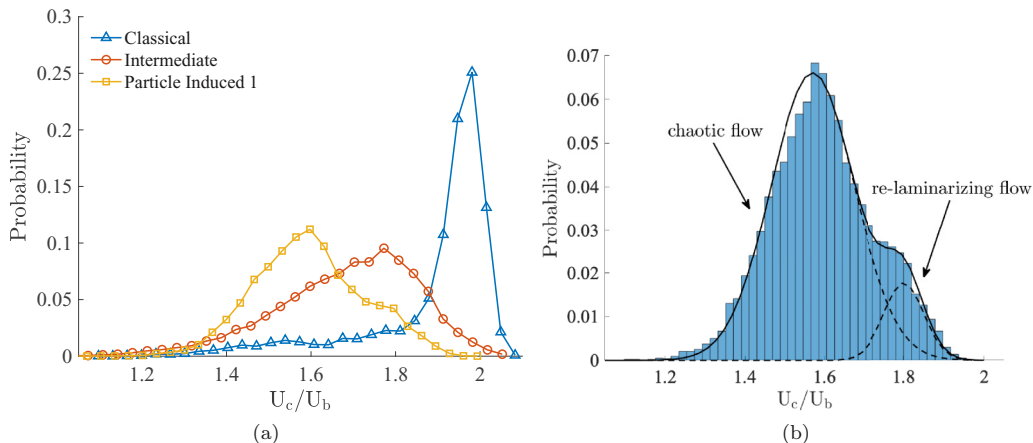
FIG. 6. (a) Centerline velocity probability distributions for different volume fractions and constant Reynolds number (≈ 2000). (b) Centerline velocity probability distribution for $\phi = 0.25\%$ and $\mathrm{Re}_s = 2005$. Isolated, relaminarizing patches are observed in this flow, which are indicated by the Gaussian distribution on the right-hand side. The main flow is indicated by the Gaussian distribution on the left-hand side.

1. Instantaneous velocity fields

Instantaneous velocity fields provide direct insight into the interaction between particles and flow structures. In Fig. 7 four typical flow fields for different Reynolds numbers are shown (see also the supplemental videos, S1–S3 [24]). Approximately one third of the measurement domain width is shown. The velocity fields (mean-subtracted) are superimposed on the raw camera images. The vector color represents the magnitude of the streamwise velocity component (u'_x/U_b). In every panel three (dispersed phase) particles are present. The white particles are overexposed, as they are in the laser light sheet, whereas black particles are located outside this light sheet and are illuminated by the LED source only.

For Re_s as low as 1010, elongated structures can first be observed in the flow. The length of these elongated structures increases for increasing Reynolds number, as can be seen for $\mathrm{Re}_s = 2005$. Here a typical elongated flow structure is present with an approximate length of $5D$. The velocity in these elongated structures can be significantly different compared to the bulk velocity; see also Fig. 9 for a quantitative description. For higher Reynolds numbers these elongated structures break down, which can be seen for $\mathrm{Re}_s = 3475$ and 5069. This will be discussed in more detail later (see Sec. IV C 3).
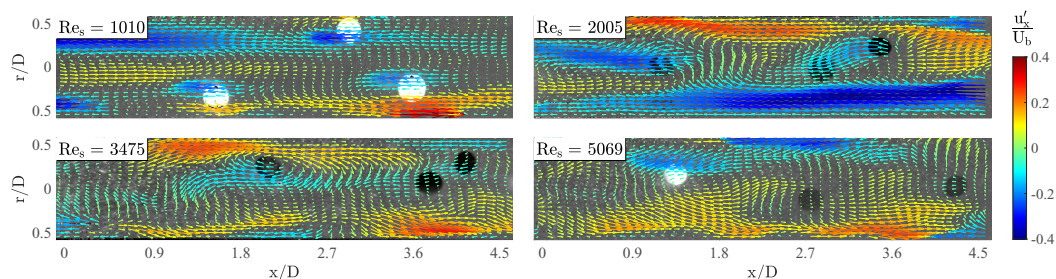

FIG. 7. Typical, instantaneous flow fields superimposed on the corresponding camera images for particle-induced transition ($\phi = 0.25\%$). The vector color represents the normalized magnitude of streamwise velocity component (u'_x/U_b). See also the supplemental videos, S1–S3 [24].
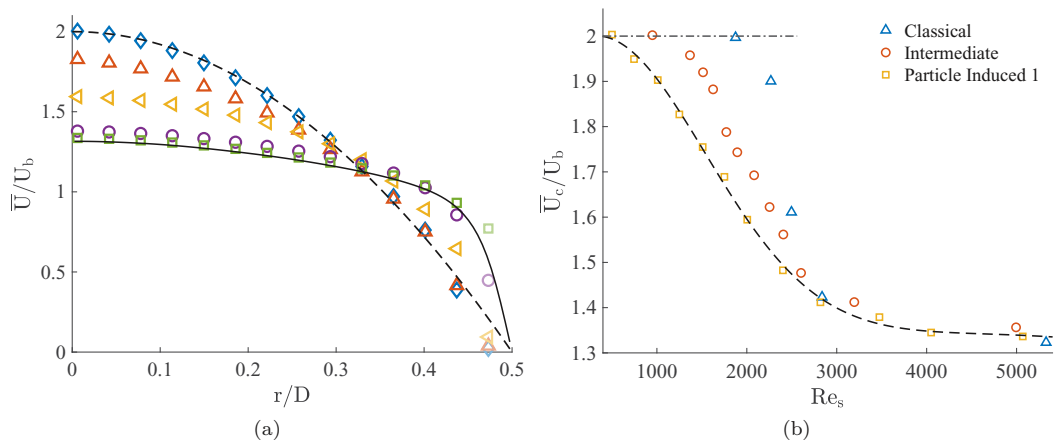
FIG. 8. (a) Average velocity profiles ($\bar{U}$), scaled with the bulk velocity for particle-induced transition ($\phi = 0.25\%$) for the following Reynolds numbers: $\diamond$ $\text{Re}_s = 500$, $\triangle$ $\text{Re}_s = 1249$, $\triangleleft$ $\text{Re}_s = 2005$, $\circ$ $\text{Re}_s = 3475$, $\square$ $\text{Re}_s = 5069$. The dashed line is the analytical solution for a laminar flow, and the continuous line is the reference data for single-phase flow with $\text{Re} = 5300$. (b) Average centerline velocities scaled with the bulk velocity as a function of Re_s. The dashed line is a double Gaussian fit to indicate the trend of the particle-induced 1 transition case.

2. Velocity and stress data

Mean velocity profiles and statistics are useful to describe this particle-induced transition. In particular the velocity statistics (i.e., root mean square of the velocity components and Reynolds stress) show the nature of transition. The mean velocity profile, $\bar{U}$, normalized with the bulk-flow velocity as a function of the pipe radius (r) is shown in Fig. 8(a). The colors represent different Reynolds numbers, which are listed in the caption. The dashed line is the analytical solution (parabola) for a laminar flow, whereas the continuous line is based on reference data for a single-phase turbulent flow with $\text{Re} = 5300$ (reproduced from Eggels et al. [25]). The markers closest to the wall are shown transparently as these data are contaminated with noise. This is mainly due to the strong velocity gradients in this near-wall region. For increasing Reynolds number the velocity profile becomes more blunted. Eventually, for $\text{Re}_s = 5069$, it approaches the reference solution for single-phase flow. This flattening behavior is shown in Fig. 8(b), where the normalized centerline velocity is shown as a function of Reynolds number. The dashed line is a double Gaussian fit to indicate the trend of the particle-induced transition case. The earlier onset to transition for an increasing volume fraction is evident in Fig. 8(b), as the flattening behavior of the laminar velocity profile (i.e., the deviation from $\bar{U}_c/U_b = 2$) starts at lower Re_s. This also shows that the transition occurs over a wider Re_s range for increasing volume fractions, as the end of the transition (i.e., the fully turbulent situation) is reached at a similar Re_s. This can be seen by the collapse of the markers for $\text{Re}_s \gtrsim 3000$.

The second-order statistics are presented in Figs. 9(a) and 9(b), where the u_x-rms and the u_r-rms data are shown, respectively. The velocity fluctuations for both the streamwise and the radial velocity component gradually increase for increasing Reynolds number. This behavior emphasizes the gradual transition for this particular transition case. Again, for $\text{Re}_s = 5069$ (green square markers) the velocity fluctuations approach the reference data for single-phase flow for $\text{Re} = 5300$.

In Fig. 10 the spatially averaged streamwise and radial rms profiles for classical and particle-induced transition cases are shown as a function of Re_s. Here $\overline{u-rms}$ is obtained from the integration
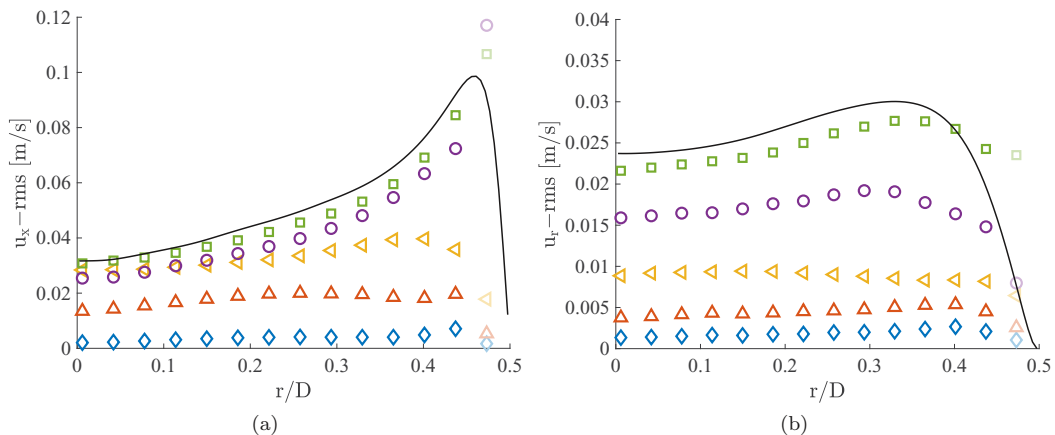
FIG. 9. (a) u_x-rms and (b) u_r-rms profiles for particle-induced transition ($\phi = 0.25\%$) and various Reynolds numbers: $\diamond$ Re$_s$ = 500, $\triangle$ Re$_s$ = 1249, $\triangleleft$ Re$_s$ = 2005, $\circ$ Re$_s$ = 3475, $\square$ Re$_s$ = 5069. The continuous line represents reference data for single-phase flow for Re = 5300.

of the profile (assuming axisymmetry), normalized by the cross-sectional area of the pipe:

$$\overline{u-rms}^2 = \frac{8}{D^2} \int_0^{D/2} \overline{u'(r)^2} \, r \, dr. \tag{2}$$

The unreliable data closest the wall (see the transparent markers in Fig. 9) are replaced by linear interpolation, assuming no-slip conditions at $r/D = 0.5$. For both transition cases the average rms-values increase for increasing Re$_s$, in agreement with the observations in Figs. 9(a) and 9(b). Note the linear increase for both the streamwise and radial $\overline{u-rms}$ component for the particle-induced transition for increasing Re$_s$. This will be elaborated upon further in Sec. V. The results from the intermediate case are not shown in this comparison; the data quality of these measurements was sufficient for mean velocity profiles, but the seeding density was too low to reliably obtain statistics of the fluctuations.

The stress budgets along the profile for particle-induced transition for various Reynolds numbers are shown in Fig. 11. These are normalized using the wall shear stress (τ_w), which is based on
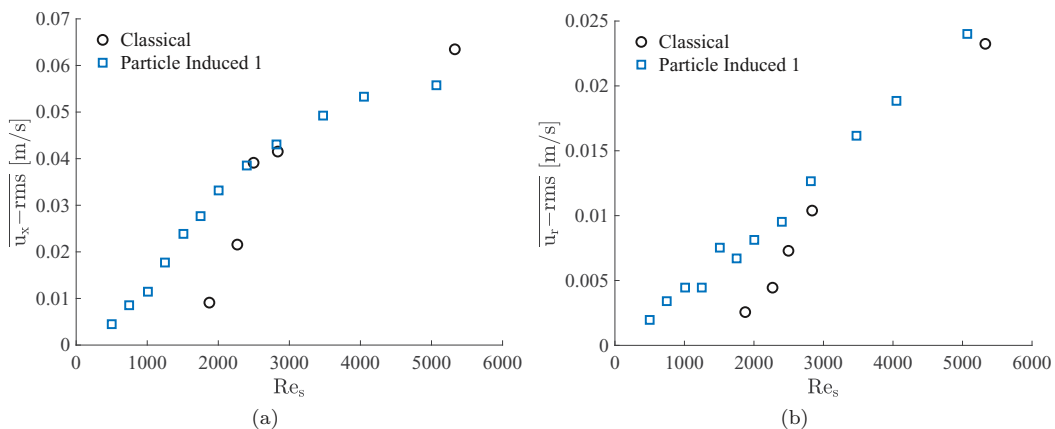

FIG. 10. (a) Averaged u_x-rms and (b) u_r-rms as a function of Reynolds number for classical ($\phi = 0\%$) and particle-induced transition ($\phi = 0.25\%$). Note the difference in vertical axis scaling.
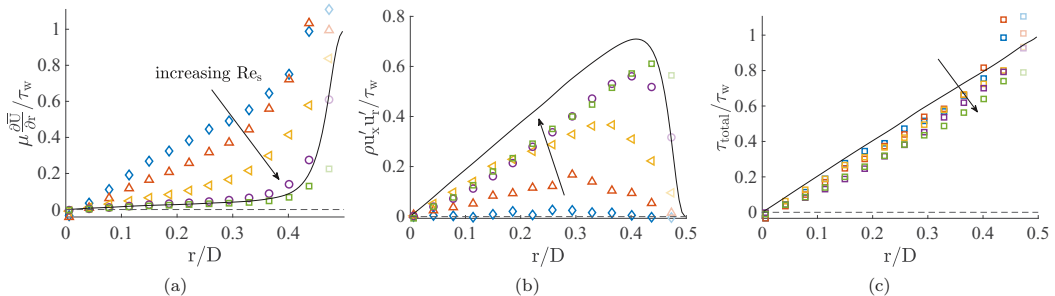
FIG. 11. (a) Normalized viscous stress, (b) Reynolds stress, and (c) total stress profiles for particle-induced transition ($\phi = 0.25\%$) and different Reynolds numbers: $\diamond$ Re$_s = 500$, $\triangle$ Re$_s = 1249$, $\triangleleft$ Re$_s = 2005$, $\circ$ Re$_s = 3475$, $\square$ Re$_s = 5069$. The direction of the arrow indicates increasing Re$_s$. The continuous line represents the reference data for single-phase flow for Re $= 5300$.

the pressure drop measurements. The viscous stress component [Fig. 11(a)] gradually decreases for increasing Re$_s$, as indicated with the arrow. The Reynolds stress component [Fig. 11(b)] gradually increases for increasing Re$_s$, showing the gradual emergence of turbulence. The total normalized stress profiles are shown in Fig. 11(c). The underestimation of the linear stress profile results from the underestimation of the Reynolds stress component ($u'_x u'_r$) as can be seen in Fig. 11(b). The deviation increases for increasing Re$_s$, due to the fixed, finite PIV resolution and the smaller flow features for higher Re$_s$.

3. Integral length scales

The experiments were not designed to resolve small-scale structures in the flow. The acquisition frequency of the camera and the spatial resolution are not sufficient to resolve the smallest scales. However, the temporal resolution of the streamwise velocity data in the transition region is sufficient to compute autocorrelation functions to characterize the larger scales in the flow. Integration of this autocorrelation function (R) yields the integral time scale, defined as

$$\mathcal{T} = \int_0^\infty R(\tau)\, d\tau. \tag{3}$$

A typical correlation function close to the pipe wall ($r/D = 0.4$), for the streamwise velocity component (u'_x) is shown in Fig. 12(a). The general decay of this correlation function is best described by an exponential function with a decay time t_0. An exponential function is fitted to the autocorrelation function, based on R_{uu} for $t \leqslant 0.1$ s. Beyond this time, the data deviates from this exponential function, which is due to insufficient convergence as a result of the limited length of the time series. Comparing numerical integration of the autocorrelation function (until $t = 0.6$ s, where the signal is decorrelated) with the analytical integration of the exponential fit gives an error less than 5% for the integral timescale. In this study the latter method is used. The integral time and length scales as a function of r/D for various Reynolds numbers are shown in Figs. 12(b) and 12(c), respectively. The local mean velocity [$\bar{U}$; see Fig. 8(a)] is used to calculate the integral length scales ($\mathcal{L}$) from the integral timescales. The integral length scales are normalized using the pipe diameter. These results confirm the previous qualitative description based on the instantaneous flow fields. To illustrate, for Re$_s = 1010$, flow structures with a length of $2D$ can be observed in the top left in the first panel in Fig. 7; see also video S1-Re 1010 [24]. These structures increase in length for increasing Reynolds number. For Re$_s = 1509$ and 2005 (average) length scales in the order of 3 to 5D are found. This is confirmed by the flow structure in the second panel in Fig. 7 and with the supplemental video S2-Re 2005 [24]. For Re$_s = 2005$, the slotting method was used to determine the length scale, to ignore the "laminar" patches. Beyond this Reynolds number the length of the
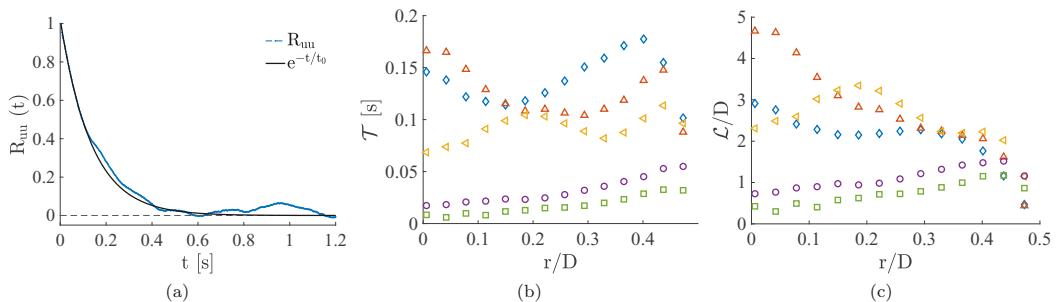
FIG. 12. (a) A typical correlation function at a radial location $r/D = 0.4$ for the streamwise velocity component. The black continuous line is an exponential function which is fitted to the data based on the first datapoints ($t \leqslant 0.1$ s). For this case a decay time is found of $t_0 = 0.14$. (b) Integral time and (c) length scales for particle-induced transition ($\phi = 0.25\%$) as a function of pipe diameter for various Reynolds numbers: $\diamond$ $\mathrm{Re}_s = 1010$, $\triangle$ $\mathrm{Re}_s = 1509$, $\triangleleft$ $\mathrm{Re}_s = 2005$, $\circ$ $\mathrm{Re}_s = 2818$, $\square$ $\mathrm{Re}_s = 3475$.

structures rapidly decreases for increasing Reynolds number. This can be seen for instance the last two panels in Fig. 7 or supplemental video S3-Re 4050 [24].

V. DISCUSSION

This study analyzes a particle-induced laminar-turbulent transition in detail using planar PIV. For small D/d ratios (5.7 in our study), even dilute systems exhibit this particle-induced transition behavior. A suspension with a volume fraction as low as 0.25% is found to be on the "edge" of this particle-induced transition behavior, while still allowing sufficient optical access to perform accurate PIV measurements. These measurements confirm what was observed qualitatively in a previous study [13], but provide quantitative information to investigate the details of the transition process. The agreement also suggests that our results for this "sweet spot" with fairly extreme parameters can likely be extrapolated to smaller particle sizes that exhibit this transition.

Our work confirms results from previous studies with relatively large particles [11] that found a decrease in Re_c with increasing volume fractions [Fig. 8(b)]. We observe an increase in the friction factor in this transitional regime [Fig. 2(a)], with the friction factor being higher than either Poiseuille or Blasius (which is technically not valid in this range). Beyond the transition region, there appears to be no major increase in the friction factor. The absence of an increase in friction beyond the transitional region is in agreement with the observations of Leskovec *et al.* [15]. They report similar transition curves for $D/d = 5.9$ (even for concentrations up to 30%). Note that this behavior is in contrast with previous studies using smaller particles: for $D/d \approx 20$ initially a drag increase was reported (until a volume fraction of $\phi \gtrsim 15\%$), beyond which the friction *decreases*, even below the Blasius curve [13,14]. Similar nonmonotonic behavior of the friction factor was also observed in channel flow using numerical simulations by Costa *et al.* [31]. They suggest that there are two competing mechanisms at play: for low volume fractions the particles induce additional friction due to the disturbances because of their finite size. For very large volume fractions, the particles attenuate the (turbulent) fluctuations. Note that our experiments are in a very dilute regime, far from, e.g., the inertial shear-thickening regime observed for higher volume fractions [32]. As the fully turbulent regime was not the focus of this paper, we refrain from speculating about the frictional drag for significantly higher Re_s.

From the PIV results, the average velocity profiles [$\bar{U}$; see Fig. 8(b)] are found to gradually change from a parabolic (laminar) to a blunted (turbulent) profile. At first sight, this result may seem trivial, as it resembles the behavior seen in the classical scenario for single-phase flows. However, there is an important distinction in the underlying physics: for single-phase flow, the flattening of the profile is an artefact of the averaging of two distinct states. The shape of the mean velocity profile

falls between these two, based on the intermittency at that given Re. For increasing Re, the amount of puffs increases, and hence the *average* profile flattens. This does not imply that the instantaneous profile resembles this average: the instantaneous profiles are either parabolic or flattened (turbulent). In the particle-laden case, the instantaneous profiles truly fluctuate around this average. This distinct behavior can be observed in Fig. 5, but also in the PDFs of Fig. 6(a).

The instantaneous velocity fluctuations around this mean profile are given by the u_x-rms and u_r-rms curves (see Fig. 9). Classical transition is characterized by an "overshoot" for u_x-rms at the centerline in the transition region (see, e.g., Fig. 6 in Trip *et al.* [33]). This overshoot again is the result of intermittency, which complicates the Reynolds decomposition due to the ambiguity of the mean velocity. As can be seen in Fig. 9, the fluctuations gradually increase for increasing Re_s, without the overshoot. This further confirms the absence of the intermittency for particle-induced transition. The gradual increase in fluctuations (and Reynolds stress) are required to sustain the flattening profiles, as they provide additional mixing.

The particles induce fluctuations, but not due to their inertia, as the Stokes time is very small for these neutrally buoyant particles. Rather, the fluctuations originate from their finite size, causing a disruption of the (parabolic) fluid velocity profile. This is evident in the top-left panel of Fig. 7. These induced velocity fluctuations u' scale with the product of the particle diameter (d) and the velocity gradient of the fluid, U_b/D. This results in the scaling: $u' \sim U_b d/D$. Throughout this study the particle-to-pipe diameter ratio is constant, which reduces this scaling to $u' \sim U_b$. Furthermore, when the bulk flow behavior is considered, the integrated velocity fluctuations ($\overline{u-rms}$) are expected to scale linearly with U_b. This linear scaling is indeed observed for the particle-induced case, as shown in Fig. 10. Here the average velocity fluctuations, $\overline{u-rms}$ increase linearly with Re_s or U_b (as D and ν are constant across each set of experiments). Beyond $Re_s \approx 2750$ for $\overline{u_x-rms}$, the behavior start to deviate from the scaling, which is likely due to the emerging turbulence as can be seen in, e.g., Fig. 11(b). This is also visible from the collapse of the classical and particle-induced measurements for $Re_s > 2750$ in Fig. 10(a). The linear scaling for $Re_s < 2750$ is absent for the classical transition case, as no particles are present in this flow.

The different nature of the particle-induced transition is also evident from the additional length scales that are identified (see Fig. 12). These length scales are associated with elongated (streamwise) structures that span several diameters. An interesting observation is that the length scale of these structures initially increases with Re_s, before decreasing for even higher Re_s. The structures are likely rooted in the fluctuations induced by the particles. The increase in length with Re_s might be explained by the hypothesis given by Matas *et al.* [11]: "With increasing Re_p, the disturbance flow caused by the particle is presumably less efficiently dissipated by viscous action, thus allowing for stronger coupling to the bulk flow." Our results support this hypothesis. Note that in our experiments the particle Reynolds number is proportional to Re_s, as we use a single D/d ratio. For larger Re_s, turbulence is most likely responsible for the (gradual) break-down of the elongated flow structures, as the critical Reynolds number for sustained turbulence is reported at 2040 [4]. Figures 10(a) and 10(b) show that this also holds for cases with particles. Beyond this Re_s, the length scales rapidly decrease to an average length, in the same order as the pipe diameter.

The observation of these relatively long structures may also have implications for computational studies. To capture these structures, longer domain sizes may be required than what is currently customary (sometimes as low as $4D$, with periodic boundary conditions [34]).

Looking at visualizations such as Figs. 4 and 5, it is tempting to correlate the location of particles with the presence of disturbances in the flow field. To investigate whether there is a correlation between particle location and flow structure, the local "kinetic energy" ($\sqrt{u_x'^2 + u_r'^2}$, where the averaging operator is over the radial direction and one pipe diameter in the streamwise direction), was correlated with the local volume fraction (ϕ). No significant correlation was found, even after varying the "filter length." This can be explained by the fact that the particles generally travel with the local flow velocity (see, e.g., video S2-Re 2005 [24]). Depending on their radial position, particles travel slower or faster compared to the bulk velocity. As the disturbances cover most of

the cross section, it is expected that they travel with approximately the bulk velocity—similar to conventional turbulent puffs [3]. As our visualizations are built by stacking consecutive recordings of a single velocity profile, they must not be interpreted as instantaneous snapshots of a large pipe segment. Particle (de-)clustering and their influence on flow structures upstream to the measurement section can not be quantified as there is no history information present in these measurements. In other words, if a disturbance is caused in the past by a cluster of particle, by the time this disturbance passes our measurement volume, the particles may have moved with respect to the disturbance (and with respect to each other). A hypothesis that can be formulated is that these disturbances have a lifetime long enough to survive without particles. Otherwise, we would see only disturbances very close to the presence of particles. Measurements capturing a larger pipe length are required to quantify the correlation between particles and disturbances.

For higher Reynolds number ($\mathrm{Re}_s = 2005$, $\phi = 0.25\%$), some "laminar" patches are observed, which are embedded in a chaotic flow [see, e.g., Fig. 6(b)]. The origin of these "laminar" patches might be rooted in the spatial particle distribution. This distribution is described by a Poisson distribution ($\lambda = 11.1$) in the measurement volume (i.e., $12D$), so statistical fluctuations are still significant. To illustrate: for 13% of the time the local concentration is twice as low as the bulk concentration. For lower concentrations the transition exhibits more classical transition behavior, with a higher fraction of laminar flow regions [see, e.g., Fig. 6(a)]. Again, this needs to be confirmed by measurements with a (much) larger field of view. The laminar patches are thus likely a result of our relatively extreme choice of parameters, needed to perform optical measurements. For smaller particles, the statistical fluctuations for a given volume fraction will rapidly decline. It is hypothesized that these laminar patches will then also disappear.

Before concluding, it is worth restating that our classification of the transition into "classical," "intermediate," and "particle-induced" types is here based on the presence or absence of certain flow features. However, these features are naturally closely linked to the integral properties, specifically the mean pressure drop. This has been confirmed by the present study, but also by previous work [13]. The transition type could therefore also be defined based on the friction factor behavior. For a given D/d ratio, and assuming a gradual increase in the volume fraction, the boundary between classical and intermediate transition can be chosen as the moment that Re_c starts deviating from the single-phase case (e.g., a 10% difference with respect to Poiseuille [13]). The boundary between intermediate and (fully) particle-induced can be defined as the moment that the friction factor monotonically decreases. This classification can serve as alternative to the qualitative description based on flow features, which requires more elaborate experiments. It also presents an alternative to classifications based on the stress budget [32], an approach requiring data far beyond most experiments.

VI. CONCLUSION

We performed a planar PIV study on a particle-induced laminar-turbulent transition case with a pipe-to-particle diameter ratio of 5.7. For a volume fraction of 0.25% the Darcy friction factor is found to monotonically decrease for increasing Reynolds number.

The particle-induced transition ($\phi = 0.25\%$) is characterized by the presence of continuous velocity fluctuations rather than the presence of puffs, which are characteristic for classical transition. The average velocity profile gradually changes from a parabola (laminar flow) to a blunted velocity profile for increasing Reynolds number. For the particle-induced transition case, the instantaneous velocity profile is fluctuating around this average profile. These velocity fluctuations, given by $u_x - rms$ and $u_r - rms$, gradually increase for increasing Reynolds number. For low Re_s this increase is proportional to the bulk velocity; this can be explained using a simple scaling argument based on the finite size of the particles. The gradual increase of the fluctuations confirms the different nature of particle-induced transition, as for classical transition an overshoot is present at the centerline for transitional cases, due to the presence of puffs.

Time and length scales of the flow structures are obtained using the autocorrelation function of the streamwise velocity component. For $\mathrm{Re}_s = 1010$, flow structures with an average integral length scale up to $3D$ are present in the flow. This length is increasing for increasing Re_s, up to an integral length scale of $5D$ for $\mathrm{Re}_s = 1509$. Beyond $\mathrm{Re}_s = 2005$ these elongated structures break down rapidly due to sustained turbulence. Due to the nature of our measurements, we cannot investigate the link between perturbations in the flow and the presence of particles.

For future work, specific measurements can provide insight in various hypotheses and open questions that were formulated in this study. Using a smaller field of view, PIV measurements can quantify the exact way these particles create perturbations in the flow. On the other hand, measurements with a (much) larger field of view will shed light on the way perturbations and particles correlate with each other. The former can also be investigated using numerical simulations, but for the latter this will be challenging due to the very large domain size.

A discussion of the role of the pipe-to-particle diameter ratio has deliberately been excluded from this study. Based on our own preliminary work and a recent study by Leskovec *et al.* [15], it is known to play a key role in deciding at which volume fraction the change in transition mechanism occurs. Optical access strongly reduces for smaller particle size (for a fixed concentration), hence insight can no longer come from PIV. We are therefore currently pursuing the role of diameter ratio using magnetic resonance velocimetry and ultrasound-based measurements.

[1] O. Reynolds, An experimental investigation of the circumstances which determine whether the motion of water shall be direct or sinuous, and of the law of resistance in parallel channels, Philos. Trans. R. Soc. London **174**, 935 (1883).

[2] B. Hof, J. Westerweel, T. M. Schneider, and B. Eckhardt, Finite lifetime of turbulence in shear flows, Nature (London) **443**, 59 (2006).

[3] D. J. Kuik, C. Poelma, and J. Westerweel, Quantitative measurement of the lifetime of localized turbulence in pipe flow, J. Fluid Mech. **645**, 529 (2010).

[4] K. Avila, D. Moxey, A. de Lozar, M. Avila, D. Barkley, and B. Hof, The onset of turbulence in pipe flow, Science **333**, 192 (2011).

[5] V. Murthy and I. Zandi, Turbulent flow of non-Newtonian suspensions in pipes, J. Eng. Mech. Div. **95**, 271 (1969).

[6] W. C. Mih, Transporting solid particles in smooth pipelines, Transp. Eng. J. ASCE **105**, 427 (1979).

[7] M. Abbas and C. Crowe, Experimental study of the flow properties of a homogenous slurry near transitional Reynolds numbers, Int. J. Multiphase Flow **13**, 357 (1987).

[8] A. Einstein, Berichtigung zu meiner arbeit: Eine neue bestimmung der moleküldimensionen, Annalen der Physik **339**, 591 (1911).

[9] J. T. Park, R. J. Mannheimer, T. A. Grimley, and T. B. Morrow, Pipe flow measurements of a transparent non-Newtonian slurry, J. Fluids Eng. **111**, 331 (1989).

[10] J. J. Stickel and R. L. Powell, Fluid mechanics and rheology of dense suspensions, Annu. Rev. Fluid Mech. **37**, 129 (2005).

[11] J.-P. Matas, J. F. Morris, and E. Guazzelli, Transition to Turbulence in Particulate Pipe Flow, Phys. Rev. Lett. **90**, 014501 (2003).

[12] Z. Yu, T. Wu, X. Shao, and J. Lin, Numerical studies of the effects of large neutrally buoyant particles on the flow instability and transition to turbulence in pipe flow, Phys. Fluids **25**, 043305 (2013).

[13] W. Hogendoorn and C. Poelma, Particle-Laden Pipe Flows at High Volume Fractions Show Transition without Puffs, Phys. Rev. Lett. **121**, 194501 (2018).

[14] N. Agrawal, G. H. Choueiri, and B. Hof, Transition to Turbulence in Particle Laden Flows, Phys. Rev. Lett. **122**, 114502 (2019).

[15] M. Leskovec, F. Lundell, and F. Innings, Pipe flow with large particles and their impact on the transition to turbulence, Phys. Rev. Fluids **5**, 112301 (2020).

[16] C. Poelma, Measurement in opaque flows: A review of measurement techniques for dispersed multiphase flows, Acta Mech. **231**, 2089 (2020).

[17] P. Costa, F. Picano, L. Brandt, and W.-P. Breugem, Universal Scaling Laws for Dense Particle Suspensions in Turbulent Wall-Bounded Flows, Phys. Rev. Lett. **117**, 134501 (2016).

[18] I. J. Wygnanski and F. Champagne, On transition in a pipe. Part 1. The origin of puffs and slugs and the flow in a turbulent slug, J. Fluid Mech. **59**, 281 (1973).

[19] I. Abdulagatov, A. Zeinalova, and N. Azizov, Viscosity of aqueous Na_2SO_4 solutions at temperatures from 298 to 573 K and at pressures up to 40 MPa, Fluid Phase Equilib. **227**, 57 (2005).

[20] MATLAB, version 9.7 (R2019b) (The MathWorks Inc., Natick, Massachusetts, 2019).

[21] L. Adrian, R. J. Adrian, and J. Westerweel, *Particle Image Velocimetry*, Cambridge Aerospace Series: 30 (Cambridge University Press, 2011).

[22] J. Westerweel, Digital particle image velocimetry: Theory and application, Ph.D. thesis, Delft University of Technology, 1993.

[23] J. Westerweel and F. Scarano, Universal outlier detection for PIV data, Exp. Fluids **39**, 1096 (2005).

[24] See Supplemental Material at http://link.aps.org/supplemental/10.1103/PhysRevFluids.6.064301 for three videos showing instantaneous velocity fields for different Reynolds numbers.

[25] J. Eggels, F. Unger, M. Weiss, J. Westerweel, R. Adrian, R. Friedrich, and F. Nieuwstadt, Fully developed turbulent pipe flow: A comparison between direct numerical simulation and experiment, J. Fluid Mech. **268**, 175 (1994).

[26] L. Benedict and R. Gould, Towards better uncertainty estimates for turbulence statistics, Exp. Fluids **22**, 129 (1996).

[27] S. B. Pope, *Turbulent Flows* (Cambridge University Press, Cambridge, 2000).

[28] W. Hogendoorn and C. Poelma, High frame rate flow measurement using ultrasound imaging velocimetry, in *Proceedings of the 13th International Symposium on Particle Image Velocimetry*, edited by C. J. Kähler, R. Hain, S. Scharnowski, and T. Fuchs (Universität der Bundeswehr München, München), pp. 972–979.

[29] W. Mayo Jr., A discussion of limitations and extensions of power spectrum estimation with burst counter LDV systems, in *Proceedings of the 2nd International Workshop on Laser Velocimetry* (Purdue University, West Lafayette, Ind., 1974), pp. 90–104.

[30] M. Tummers and D. Passchier, Spectral analysis of biased LDA data, Meas. Sci. Technol. **12**, 1641 (2001).

[31] P. Costa, L. Brandt, and F. Picano, Near wall turbulence modulation by small inertial particles, arXiv:2102.11597 (2021).

[32] I. Lashgari, F. Picano, W.-P. Breugem, and L. Brandt, Laminar, Turbulent, and Inertial Shear-Thickening Regimes in Channel Flow of Neutrally Buoyant Particle Suspensions, Phys. Rev. Lett. **113**, 254502 (2014).

[33] R. Trip, D. Kuik, J. Westerweel, and C. Poelma, An experimental study of transitional pulsatile pipe flow, Phys. Fluids **24**, 014103 (2012).

[34] M. N. Ardekani, L. Al Asmar, F. Picano, and L. Brandt, Numerical study of heat transfer in laminar and turbulent pipe flow with finite-size spherical particles, Int. J. Heat Fluid Flow **71**, 189 (2018).